

Modeling OH transport phenomena in cold plasma discharges using the level set method

Mehrdad SHAHMOHAMMADI BENI¹, Wei HAN (韩伟)^{2,3} and K N YU (余君岳)¹

¹Department of Physics, City University of Hong Kong, Tat Chee Avenue, Kowloon Tong, Hong Kong, People's Republic of China

²Center of Medical Physics and Technology, Hefei Institutes of Physical Sciences, Chinese Academy of Sciences, Hefei 230031, People's Republic of China

³Collaborative Innovation Center of Radiation Medicine of Jiangsu Higher Education Institutions and School for Radiological and Interdisciplinary Sciences (RAD-X), Soochow University, Suzhou 215006, People's Republic of China

E-mail: peter.yu@cityu.edu.hk

Received 30 September 2018, revised 17 January 2019

Accepted for publication 22 January 2019

Published 26 March 2019



CrossMark

Abstract

Cold atmospheric plasmas (CAPs) have attracted considerable interest in the field of plasma medicine. Generated reactive species such as hydroxyl (OH) species play an important role in applications of CAPs. Transportation of OH species towards the target and distribution of these OH species in the plasma plume play an important role in the applications of plasma medicine. In the present work, a computational model was built to simulate the transportation and distribution of OH species in CAP discharges, which was based on the level set method to dynamically track the propagation of plasma carrier gas in air. A reaction term was incorporated for the OH species. The OH species tended to diffuse around the main stream of the carrier gas, and thus covered larger radial and axial distances. A CAP discharge onto a skin layer led to the largest accumulation of OH species at the central part of the exposed area. The distribution of OH species on the skin was asymmetric, which agreed with experiments. The computational model itself and the obtained results would be useful for future development of plasma medicine.

Keywords: cold atmospheric plasmas, plasma medicine, two-phase flow, diffusion, level set method

(Some figures may appear in colour only in the online journal)

1. Introduction

The field of plasma medicine has been progressing rapidly in recent years [1–3]. The employment of cold atmospheric plasmas (CAPs) has been found to be promising in plasma medicine, materials processing and surface treatment [4–21]. CAPs could be generated through (1) a dielectric barrier discharge (DBD) and (2) a plasma jet, including various reactive species such as OH. CAPs could be based on different working gases, such as (1) noble gas, (2) N₂ and (3) air [22]. A room temperature plasma jet could be easily generated using a noble gas as the working gas, when compared to N₂ or air [23]. Different types of noble gas CAP jets have been

reviewed [24–30]. The composition of reactive species in CAPs could be changed by regulating the voltage, frequency, working and feeding gases, and humidity [31]. CAPs have shown significant potential for cancer therapy [32–34], tooth bleaching [19], wound healing [35, 36], inactivating microorganisms [37], improving the performance of polymers [38] and enhancing the adhesion between polymeric joint-replacement materials and bone [39]. Previously, Li *et al* [40] studied a microwave jet plasma system which generated nitric oxide and compared the effects on HeLa cells with those from DBD plasma. The authors noted that atmospheric pressure non-thermal plasma was an effective and safe method for clinical cancer therapy. In a separate study, Ishaq *et al* [41]

reviewed the mechanisms and impact of atmospheric pressure plasmas for efficient anticancer therapies. The reactive species generated by atmospheric pressure plasma affected the metabolism of the cancer cells and caused detrimental effects on the proliferation of tumor cells. More recently, Lu and Ostrikov [42] comprehensively reviewed the features of atmospheric pressure plasmas. The plasma bullet feature was also discussed. In particular, the plasma tended to propagate in the direction of the gas flow. The repeatable and regular features of atmospheric pressure plasma were noted. It was proposed that the high concentration of seed electrons controlled the threshold at which an atmospheric pressure plasma plume showed a distinctive repeatable propagation mode.

To help understand the underlying mechanisms of CAPs, and to facilitate future development of plasma medicine using CAPs, a computational model which could accurately explain and predict the transportation and distribution of reactive species in CAPs would be indispensable. The present work was devoted to the development of such a computational model. Schröder *et al* [43] was one of the pioneer groups who developed a parameterized model, which could be used to simulate the species densities generated by a plasma needle and the corresponding heat transfer to a skin layer. However, the plasma plume and its subsequent transportation to the target were not examined.

Experimental data should be available to provide validation of the developed computational model. In a recent study, Yue *et al* [23] performed experiments to reveal variations in concentrations of reactive species, such as hydroxyl (OH) species, for five different CAP devices through laser induced fluorescence (LIF) spectroscopy, which provided useful data for validation of a computational model. As such, in the present work, a computational model was built to simulate the transportation and distribution of OH species in CAP discharges, which was based on the level set method to dynamically track the propagation of plasma carrier gas in air. A reaction term was incorporated to account for the OH species. It was previously established that OH species had a lifetime of milliseconds (ms) in helium atmospheric plasma jets [23], and there was a minor decrease (25%) in OH concentrations at 1 ms in the afterglow due to termination reactions and some by diffusion [44].

We previously investigated the interaction between a plasma plume and a skin layer and the associated heat transfer mechanism using the phase field method [45]. We also examined the interaction of a plasma plume with a water medium [46] and with blood for leukemia treatment [47] using the level set interface tracking method. These studies highlighted the importance of fluid-dynamics analysis for CAP applications. In the present work, we extended our previously developed model [46, 47] to simulate the transportation of OH species in CAP discharges using the finite element method (FEM). Propagation of the plasma plume discharged out of the nozzle was tracked in air using the level set method. Transportation of the OH species in the plasma

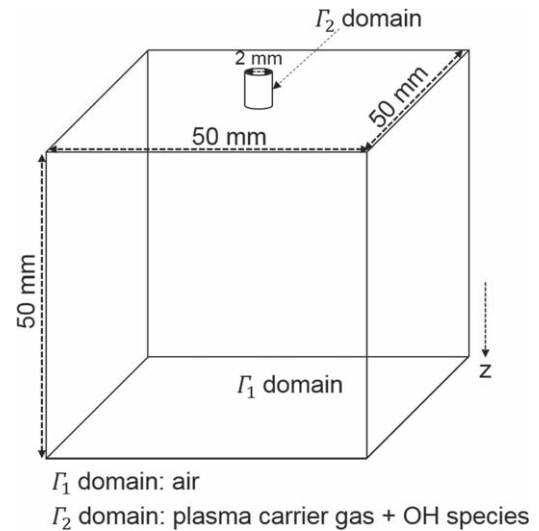


Figure 1. A schematic diagram showing the modeled system setup with dimensions. (Note: The chamber (Γ_1 domain) was initially filled with air at atmospheric pressure and all surfaces were considered to be exposed to open air (i.e. they behaved as outlets). The nozzle (Γ_2 domain) initially contained He gas, which allowed us to initialize the level set variable at the boundary that attached the nozzle to the chamber. The air in the chamber was assumed to be initially at rest and the plasma carrier gas was injected into the air domain at a specific flow rate).

plume and air by both diffusion and convection was also considered.

2. Materials and methods

2.1. Mathematical models and system setup

The system was modeled in a three-dimensional (3D) Cartesian coordinate system using the FEM technique. A rectangular chamber (domain Γ_1 in figure 1) was modeled with dimensions of $50 \times 50 \times 50 \text{ mm}^3$, with a cylindrical nozzle (domain Γ_2 in figure 1) having an inner diameter of 2 mm attached to the center of its surface along the positive z -axis. The chamber was initially filled with air at atmospheric pressure and all surfaces were considered to be exposed to open air (i.e. they behaved as outlets). The nozzle initially contained He gas, which allowed us to initialize the level set variable at the boundary that attached the nozzle to the chamber. The air in the chamber was assumed to be initially at rest and the plasma carrier gas was injected into the air domain at a specific flow rate Q .

The present system contained the plasma carrier gas (He gas) and air. Propagation of the plasma carrier gas in air was described using the level set function as

$$\frac{\partial \phi}{\partial t} + \mathbf{u} \cdot \nabla \phi = \gamma \nabla \cdot \left(\varepsilon \nabla \phi - \phi(1 - \phi) \frac{\nabla \phi}{|\nabla \phi|} \right) \quad (1)$$

where γ was introduced for better numerical stability by reducing the oscillations in the level set function and at the same time keeping the interface thickness constant. The level

set method was an interface capturing method widely used in two-phase flow problems. Equation (1) described the level set function that was coupled to the fluid-dynamics module (i.e. physics model) through the velocity field \mathbf{u} . In equation (1), ϕ represented the level set variable that varied between 0 and 1 at either side of the interface of the two fluids involved in the system (i.e. air and plasma plume). The level set function shown in equation (1) was taken from the previous work of Olsson *et al* [48, 49]; this was expressed as the so-called ‘stabilized advection’ that tended to stabilize the profile across the interface in the direction normal to the interface itself. Using this equation, good accuracy, conservation and convergence were achieved [48, 49]. The Navier–Stokes momentum and continuity equations were also used:

$$\rho \frac{\partial \mathbf{u}}{\partial t} + \rho(\mathbf{u} \cdot \nabla)\mathbf{u} = \nabla \cdot [-p\mathbf{I} + \mu(\nabla\mathbf{u} + (\nabla\mathbf{u})^T)] + F \quad (2)$$

$$\frac{\partial \rho}{\partial t} + \nabla \cdot (\rho\mathbf{u}) = 0 \quad (3)$$

where ρ was the density, P was the pressure, \mathbf{u} was the velocity field and F was the total force acting on the components in the system. The present model contained input and output boundaries. The input came from the inlet nozzle that pumped plasma into the air chamber. The side boundaries enclosing the air chamber were set to be outlets. The mass loss was taken into account through the continuity equation shown in the differential form in equation (3). The rate of mass entering the system was equal to the rate of mass leaving plus the mass accumulating within the system.

Moreover, F could be mathematically represented as $F = \rho g + F_{st} + F_{vf}$, where ρg was the body force, while F_{st} and F_{vf} represented the surface tension and volume force, respectively. For a system consisting of two phases, the total force was added to the whole computational domain in which the two phases were present. Similar mathematical approaches were employed in our previous works [46, 47, 50]. The Navier–Stokes equations were solved for each phase. For a multiphase domain, the physical properties such as density (ρ) and dynamic viscosity (μ) varied from phase 1 to 2 over the interface as $\rho = \rho_1 + (\rho_2 - \rho_1) \cdot \phi$ and $\mu = \mu_1 + (\mu_2 - \mu_1) \cdot \phi$, where ρ_1 and ρ_2 were the dimensionless densities of phases 1 and 2, respectively, while μ_1 and μ_2 were the dimensionless viscosities of phases 1 and 2, respectively [48].

Here, we focused on the transportation of OH species. The level set function was fully coupled with equation (4)

$$\frac{\partial c_{OH}}{\partial t} + \nabla \cdot (-D_{OH}\nabla c_{OH}) + \mathbf{u} \cdot \nabla c_{OH} = S_{OH} + R_{OH} \quad (4)$$

which described the transportation of OH species through diffusion and convection, where c_{OH} was the concentration of OH species, D was the diffusion coefficient, \mathbf{u} was the velocity field, S_{OH} and R_{OH} were the source and reaction terms of the OH species (described below using equation (5)). The ∇ operator in the 3D coordinate system could be represented as $\nabla = \left(\frac{\partial}{\partial x}, \frac{\partial}{\partial y}, \frac{\partial}{\partial z}\right)$. The common variable for coupling the level set function and fluid dynamics was the

Table 1. Some major OH reactions in helium atmospheric pressure plasmas and the corresponding reaction rate coefficients. Here, $f(T_e)$ indicates that the rate coefficient is obtained from electron energy distribution (EED) using the corresponding cross section [51]).

Reaction	Rate coefficient ($\text{cm}^3 \cdot \text{s}^{-1}$)
$e + \text{H}_2\text{O} \rightarrow \text{OH} + \text{H}^-$	$f(T_e)$
$\text{H}^- + \text{O} \rightarrow \text{OH} + e$	1×10^{-9}
$\text{O}^- + \text{H} \rightarrow \text{OH} + e$	5×10^{-10}
$\text{He}^* + \text{OH} \rightarrow \text{OH}^+ + \text{He} + e$	7.8×10^{-10}
$\text{He}_2^* + \text{OH} \rightarrow \text{OH}^+ + 2\text{He} + e$	6×10^{-10}
$\text{He}^+ + \text{OH} \rightarrow \text{O}^+ + \text{H} + \text{He}$	1.1×10^{-9}
$\text{He}_2^+ + \text{OH} \rightarrow \text{OH}^+ + 2\text{He}$	1.2×10^{-9}

velocity field \mathbf{u} . After coupling with equation (4), the convection term would depend on the flow of the plasma carrier gas in air. In equation (4), $\partial c_{OH}/\partial t$ and ∇c_{OH} described the temporal and spatial changes in the concentration of OH species after they were released from the source.

Reactions in the system would reduce the concentration of OH species. In a previous study, the concentration of OH species was found to have reduced by 25% after 1 ms in the plasma afterglow [44]. Based on this information, the temporal change in the concentration of OH species (c_{OH}^*) due to their reactions (hereafter referred to as the reaction term) was modeled through a decay rate λ in the form

$$c_{OH}^* = c_{OH}e^{-\lambda t} \quad (5)$$

where c_{OH} was the concentration of OH species without considering the reactions. The reaction term defined in equation (5) was solved over the grid for each spatial point, i.e. the concentration of OH species for each spatial point in the plasma plume or air was determined for each time interval. Some major reactions of the OH species in helium atmospheric pressure plasmas and the corresponding reaction constants are given in table 1. These reactions were taken from the previous work of Liu *et al* [51]. Interested readers can refer to [51] for the original list of reactions.

The system was solved through finite elements with a finite number of nodes in space, so it was important to find the optimal grid/mesh size, i.e. as fine as practically achievable, to give accurate results. Three different (from coarser to finer) grid sizes were studied, with information provided in the section on the computation scheme below. The present model could be used for modelling oxygen and its species. However, appropriate diffusion coefficients for O species would need to be input into the model.

The movement of OH species, independently of the carrier gas flow, was controlled by diffusion, while the movement of these OH species following the flow of the carrier gas (e.g. from the source into other domains) was controlled by convection. Both diffusion and convection could be referred to as ‘transport’ mechanisms and played key roles in determining the distribution of OH species, with the relative importance related to the ambient medium and concentration gradient (affecting diffusion) and the flow rate (affecting convection).

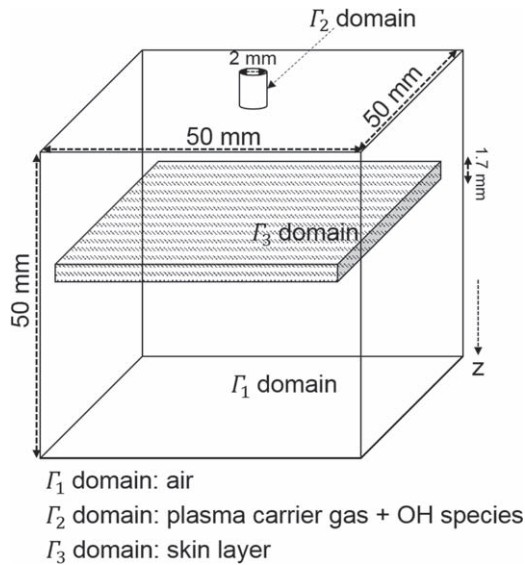


Figure 2. A schematic diagram showing the modeled system setup with dimensions in the presence of a skin layer.

The fluxes of OH species were defined to ensure the flow of these species from the nozzle along the z -axis, and to accurately control the distribution of these species. The largest inflow concentration was set to be 1 mol m^{-3} , which made it easier to score the non-dimensionalized and normalized forms of concentration of OH species in the system. Three different concentration influxes were used to obtain accurate distributions of the OH species at the nozzle outlet, which ensured that the predicted concentration gradients were comparable to those obtained experimentally. The diffusion coefficient D of the OH species was set as $0.25 \text{ cm}^2 \text{ s}^{-1}$ [52], which controlled the rate at which these species were transported.

2.2. Skin layer modeling

As regards CAP treatment of skin related diseases, the concentration and spatial distribution of reactive species (e.g. OH species) over the skin would determine the treatment effectiveness. Experimental determination of the spatial distribution of reactive species is tedious. In the present work, the concentrations of OH species over a skin layer were determined for two flow rates, namely, (i) 1 L min^{-1} and (ii) 2 L min^{-1} , and for each flow rate three nozzle-to-skin distances were considered, i.e. (i) 3 mm, (ii) 4 mm and (iii) 5 mm. Figure 2 schematically shows the system setup in the presence of a skin layer (domain Γ_3). The dimensions of the modeled skin layer were $40 \times 40 \times 1.7 \text{ mm}^3$ and all the boundaries were set to be no-slip. In fact, the skin layer acted as a solid body and the plasma carrier gas interacted with its surface. In the present study, for simplicity, we assumed the whole skin layer as a dry dielectric with a no-slip boundary condition at its surface. Due to the no-slip boundary condition, the skin layer exerted a retarding force on the carrier gas flow and the speed at the skin surface was zero. Under the no-slip boundary condition, the OH species would not be further transported upon reaching the

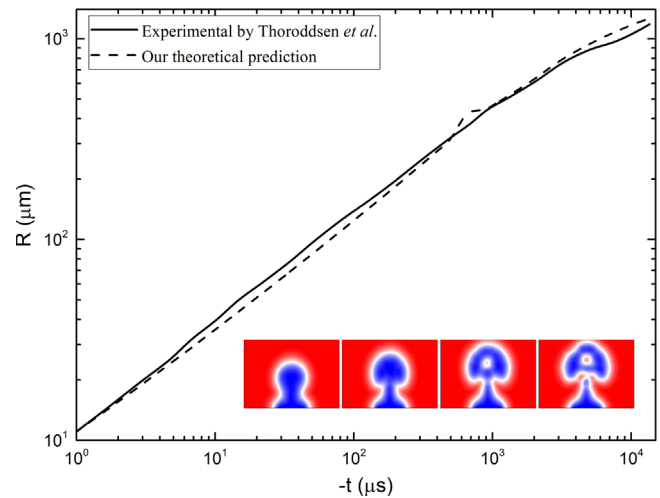


Figure 3. A comparison between the variations in the neck radius versus time leading to pinch-off obtained experimentally [53] and predicted using our model. The inset shows the sequence of air bubble pinch-off.

skin surface and could be treated as having stuck to the skin surface (i.e. with a sticking coefficient of 1). A discussion on heat transfer between the skin and the carrier gas and subsequent dispersion of the carrier gas over the skin layer can be found in our previous work [45].

2.3. Computation scheme

The present model was numerically solved in parallel on a supercomputer consisting of dual Intel Xeon E5-2630 v3 2.40 GHz CPUs. The system was solved for 0.01 s with a time step of 10^{-5} s . Employing longer time steps was possible, but significantly longer time steps might prevent the model from converging to the solution effectively. The finest time step would be recommended for the available computational resources. Three different grids/meshes were studied, namely (1) grid 1, (2) grid 2 and (3) grid 3, which consisted of 9745, 24 121 and 69 814 domain elements, respectively, and which needed average overall computation durations of $\sim 36 \text{ min}$, $\sim 52 \text{ min}$ and 6 h , respectively.

3. Results and discussion

3.1. Validation

The present model consisted of two parts, namely, (1) a two-phase flow and (2) diffusion. We validated the two-phase flow part of the code with a previously performed experiment involving the pinch-off of an air bubble under water [53]. The variations in the neck radius versus time obtained experimentally were compared with those predicted using our model, and good agreement was achieved as shown in figure 3. In addition, the present model could successfully capture the interface between air and water. The comparison showed that the two-phase flow part of the model could accurately simulate two-phase flow problems. The one-dimensional (1D) diffusion equation was also solved

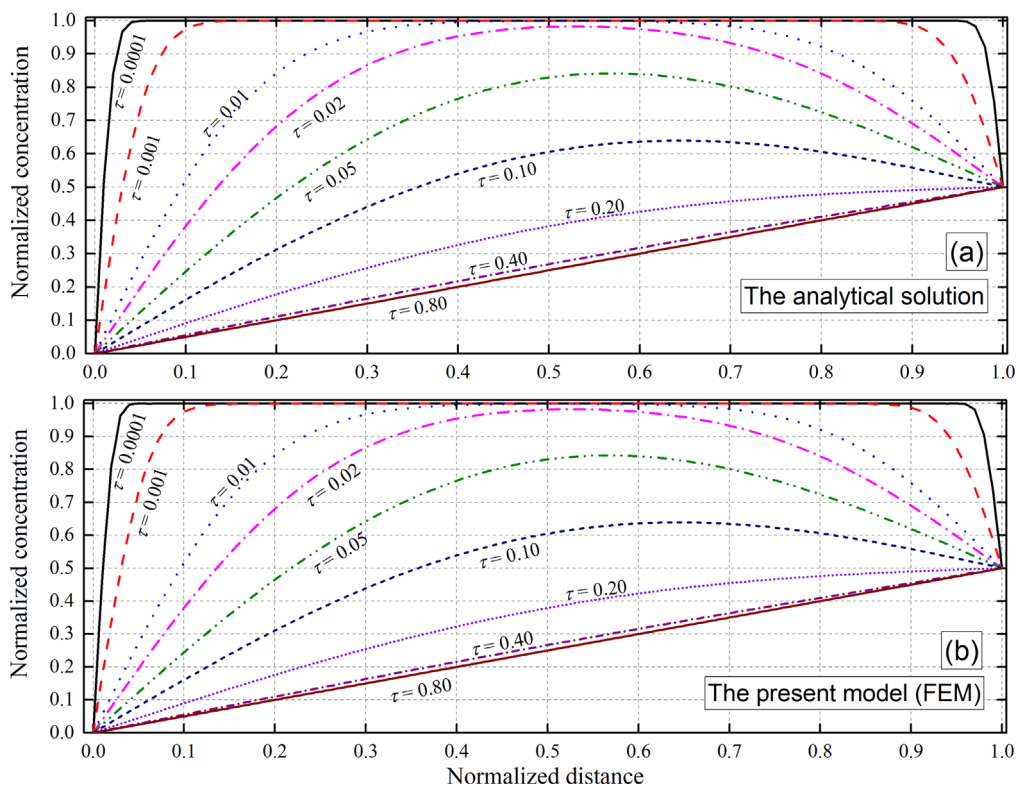


Figure 4. Variations in normalized concentration versus normalized distance at different non-dimensionalized time steps (τ) obtained from (a) analytical solution and (b) the FEM model.

analytically (see appendix A). The predicted temporal and spatial distributions of OH species using our model were compared with the analytically obtained results for $c_L = 0$ and $c_R = 0.5$ (see appendix A for definitions) in figure 4 and a remarkable agreement was achieved.

3.2. Fluid-dynamics analysis of CAP discharges

The volume fractions of plasma carrier gas from the nozzle outlet up to 50 mm away were obtained for the flow rate of 1 L min^{-1} . These volume fractions were scored for the central and four peripheral axes (i.e. averaged over a line extending from the nozzle outlet up to the end of the Γ_1 domain) (see figure 1). The variations in volume fraction of the carrier gas versus time are shown in figure 5. Initially, Γ_1 did not contain any carrier gas, i.e. the volume fraction was zero. Upon injection of carrier gas into Γ_1 , the volume fraction started to increase with time almost linearly. An interesting feature was that the volume fraction along the axis of the nozzle was higher compared to those along the peripheral points (see the inset in figure 5). This difference was attributed to the no-slip boundary condition for the nozzle walls. The adhesion between the fluid (i.e. plasma carrier gas) and the solid (i.e. nozzle walls) led to a retarding force on the carrier gas flow along the nozzle periphery, so the axial flow speed increased to compensate for the reduction in the peripheral flow speed. Hence, the carrier gas flow rate along the nozzle axis increased, and a larger volume of carrier gas could be injected into Γ_1 from the axis when compared to the periphery. The largest plasma carrier gas volume fraction was ~ 0.032 and

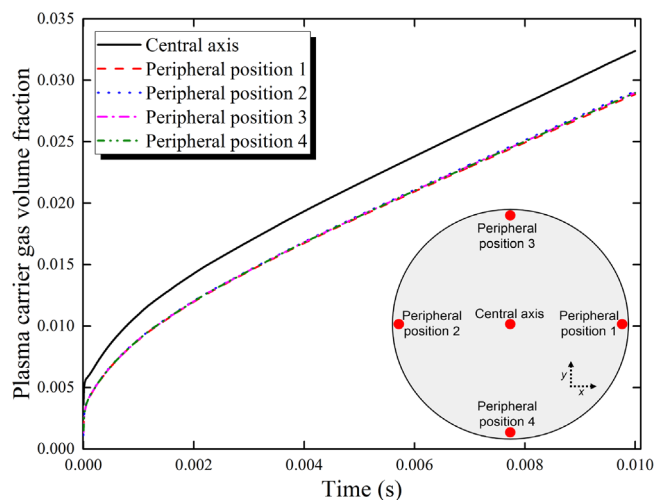


Figure 5. Volume fraction of plasma carrier gas versus time at different locations of the nozzle for the flow rate of 1 L min^{-1} along the axis extended up to 50 mm away. The inset shows the locations in/around the nozzle for the measurements.

~ 0.029 along the axis and periphery of the nozzle, respectively. The carrier gas volume fractions at the periphery were close to one another (see figure 5), which reflected the ‘isotropy’ of the carrier gas flow out of the nozzle in the presence of ambient air. In summary, plasma discharges in air without external opposing forces (i.e. forces disturbing the flow) followed a straight trajectory (see experimental observations in figure 11), with the axial flow leading the propagation of the carrier gas in air. In fact, the flow of the carrier gas was in the

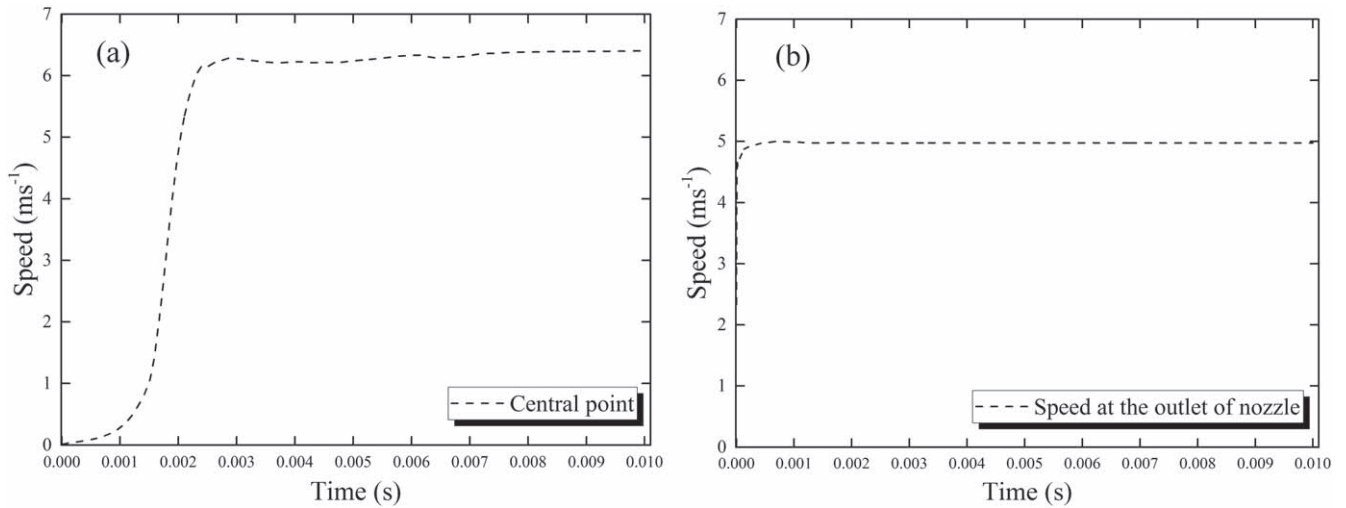


Figure 6. Variation of (a) axial carrier gas speeds versus time at a point 5 mm away from the nozzle outlet and (b) speed of the carrier gas at the nozzle outlet versus time.

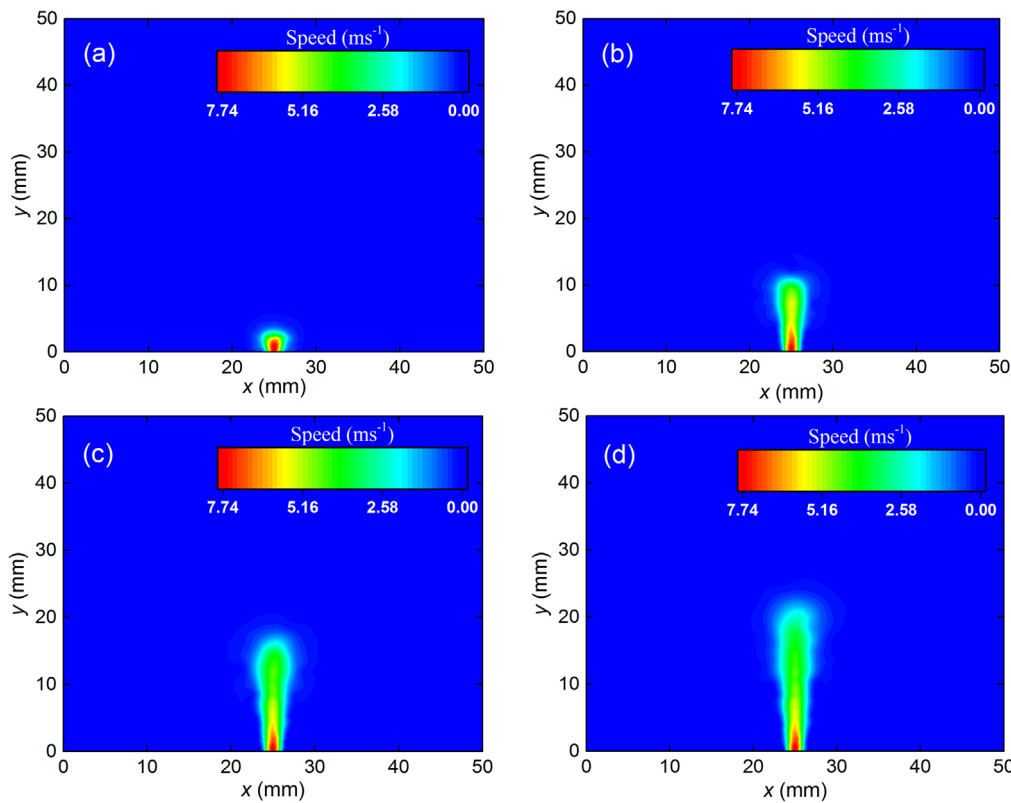


Figure 7. Speed distribution created in the air domain due to plasma discharge at (a) 0.001, (b) 0.004, (c) 0.007 and (d) 0.01 s.

laminar regime ($Re \approx 8.65 \times 10^{-4}$ at 1 L min^{-1} flow rate in the nozzle), and formation of a turbulent flow was not observed.

The axial flow speeds at 5 mm away from the nozzle outlet in Γ_1 for the flow rate of 1 L min^{-1} was determined. As shown in figure 6(a), the axial flow speed increased with time and it started to reach a constant value for $t > 0.0025 \text{ s}$.

The coordinates (in mm) of the point used to score the axial speed were (25, 25, 5). To ensure a steady-state flow of carrier gas from the nozzle, the discharge speed from the nozzle outlet into Γ_1 was obtained for the flow rate of

1 L min^{-1} . As shown in figure 6(b), the speed of the carrier gas did not vary with time. The speed out of the nozzle did not vary with time. A similar scenario was used to ensure a steady-state flow of carrier gas in our previous work [47]. It is remarked here that the final conclusion can be accurately drawn only under the steady-state flow of carrier gas.

The distributions of speed in the middle of the Γ_1 domain along the axis perpendicular to the nozzle outlet for the flow rate of 1 L min^{-1} , obtained at 0.001, 0.004, 0.007 and 0.01 s, are shown in figure 7. Apparently, regions farther away from the outlet nozzle were affected for longer plasma discharges.

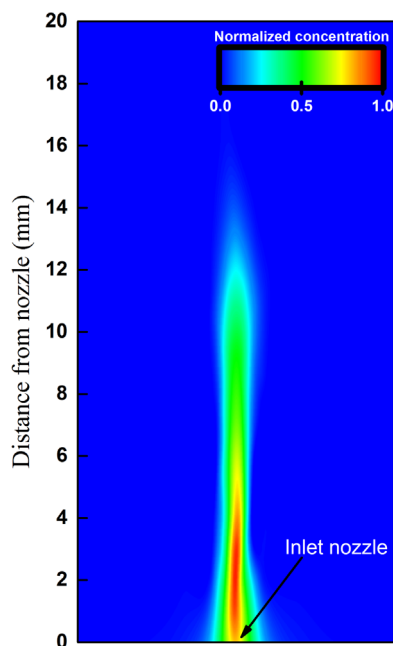


Figure 8. Spatial distribution of OH species in the carrier gas and the surrounding air.

The speed distribution was important in that it determined the dispersion and transport of the reactive species in the domain in which the plasma was discharged.

3.3. Transportation and distribution of OH species

The OH species were transported out of the nozzle through convection of the carrier gas as well as diffusion. The spatial distribution of OH species was determined for the flow rate of 1 L min^{-1} , as shown in figure 8. The concentration was highest near the nozzle outlet, and extended up to $\sim 5 \text{ mm}$. The OH species tended to diffuse around the main stream of the carrier gas and covered larger radial and axial distances. Remarkably, a similar spatial distribution of OH species was experimentally obtained using LIF spectroscopy [23]. Interestingly, the OH species were not dispersed in air, but were accumulated around the carrier gas. The OH species were initially launched in the carrier gas, so the velocities of these species were mainly controlled by the velocity of the carrier gas, which led to stronger cohesion between the species and the carrier gas when compared to air (mainly through convection). Therefore, the OH species would mainly accumulate around the carrier gas that tended to advect them in 3D space. In addition, a smooth transition was achieved for the interface between the OH species and air, as shown in figure 8.

The variations in the concentration of OH species along the nozzle axis were obtained and compared with experimental data for devices 1, 4 and 5 in figure 9(a), and for devices 2 and 3 in figure 9(b) (see [23] for information on the five devices). The theoretical predictions were in good agreement with the experimental data. The five devices included in [23] could be classified into two categories,

namely, category 1 (devices 1, 4 and 5), which included devices with the ground ring electrode to enhance discharge inside the dielectric tube, and category 2 (devices 2 and 3), which included devices with only a pin electrode but not the ground ring electrode so formation of the species inside the device was minimized [23]. For category 1, the enhancement of discharge inside the dielectric tube weakened the electric field along the plasma plume in open space, which resulted in a lower output of reactive species, so the peak OH concentrations occurred at smaller distances ($\sim 2 \text{ mm}$) from the nozzle outlet when compared to category 2 (2–3 mm), as shown in figure 9. Our simulations employed the same maximum source strength of 1 mol m^{-3} for devices in both categories 1 and 2. However, different distributions of influxes were needed for devices in categories 1 and 2, since production and reactions of reactive species were not considered. These influx distributions determined the initial distributions of OH species that were already generated and were residing in the dielectric tube. The results in figure 9 demonstrated that the present multiphysics model could accurately determine the transportation and distribution of OH species in CAP discharges. Some discrepancies between the predictions and experimental results were noticed for coarser grid sizes (i.e. grid 1), which however were minimized for finer grid sizes.

3.4. Spatial distribution of OH species over a skin layer

A CAP discharge onto a skin layer led to dispersion of reactive species over the skin surface, as shown in figure 10. Figure 10 also shows that the plasma followed a straight trajectory in air in the absence of external opposing forces. The snapshot aimed to demonstrate CAP discharge onto the skin, but not to compare the generation of OH species from our model and the experiment. Yonemori and Ono [54] used similar images of discharge towards and along a glass surface with a helium flow to demonstrate the dispersion of a CAP on a solid surface with no intention of comparing the method and location of OH species production. The spatial distributions of OH species over the skin layer (Γ_3 in figure 2) (average value of the variable c_{OH} was scored over the nodes on the skin surface) were determined for nozzle-to-skin distances of 3, 4 and 5 mm, and for the carrier gas flow rate of 1 L min^{-1} (shown in figure 11) and 2 L min^{-1} (shown in figure 12).

As shown in figure 11, the skin area exposed to the maximum concentration of OH species was underneath the nozzle outlet, for all studied nozzle-to-skin distances. However, when the nozzle-to-skin distance increased, the concentration of OH species on the skin layer decreased, which agreed with the results in figure 9. Interestingly, the exposed area on the skin layer was reduced when the nozzle-to-skin distance increased, which was attributed to the decrease in the speed of the carrier gas with increasing distance from the nozzle outlet, and thus smaller dispersion of the OH species over the skin layer. The trend was also compatible with the findings of Luan *et al* [55] that when polystyrene polymer

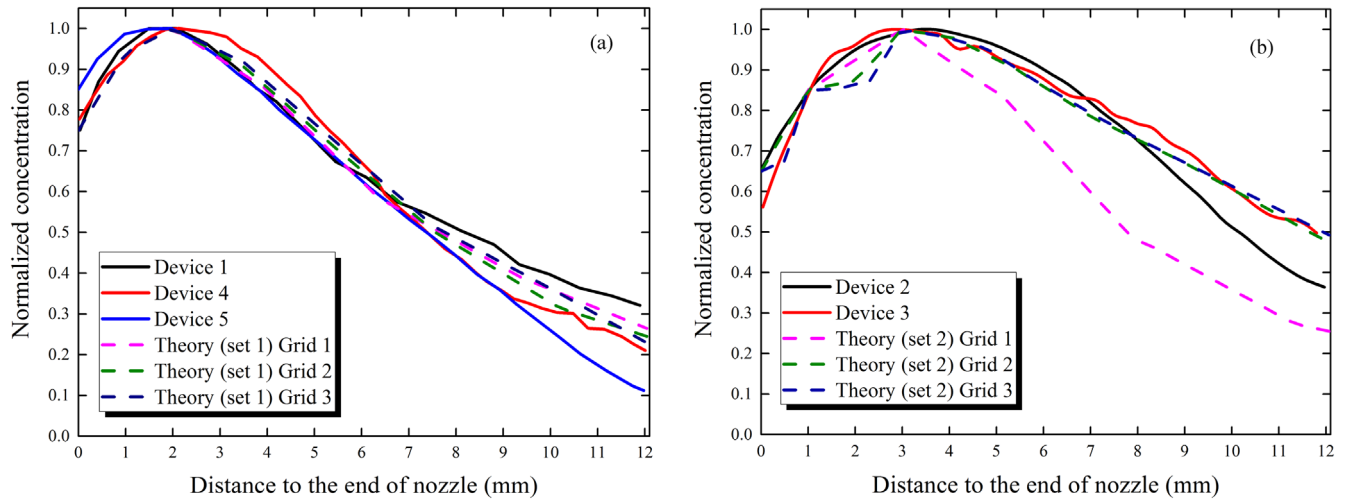


Figure 9. Variations in concentrations of OH species versus axial distance from the nozzle outlet: (a) for devices with the ground ring electrode and (b) for devices with only a pin electrode. The experimental data were taken from [23].

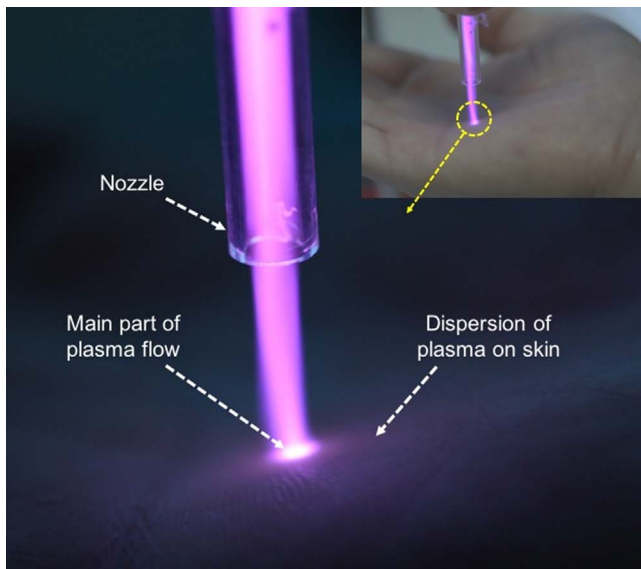


Figure 10. CAP discharge onto a skin layer.

films were exposed to CAP discharges, the polymer etch rate decayed exponentially with the nozzle-to-surface distance. These results also highlighted the important role played by nozzle-to-surface distance in the interaction between CAPs and surfaces.

As shown in figure 12, when the flow rate of the carrier gas was increased to 2 L min^{-1} , the exposed area on the skin surface increased accordingly. Interestingly, however, the exposed area was almost independent of the nozzle-to-skin distance. For larger flow rates of the carrier gas, the CAP discharge could reach the skin layer effectively, so the OH species transported through convection could distribute over the skin layer. On the other hand, the concentration of OH species decreased with increasing nozzle-to-skin distance, which was attributed to the decrease in the concentration of OH species with increasing distance from the nozzle outlet.

On the other hand, the size of the exposed area on the skin increased with the flow rate of the carrier gas. From figures 11(a) and 12(a), the exposed areas were ~ 193 and $\sim 342 \text{ mm}^2$ for carrier-gas flow rates of 1 and 2 L min^{-1} , respectively (assuming circular exposed areas for simplicity). The asymmetric distributions of OH species on the skin (i.e. inferred from the shape of exposed areas in figures 11 and 12) were also interesting, which was compatible with experimental observations of plume dispersion, as shown in figure 10. As such, solving the problem in 3D was well justified and strongly recommended.

4. Summary and conclusions

In the present work, a model was built to simulate the transportation and distribution of OH species in CAP discharges, which was based on the level set method to dynamically track the propagation of plasma carrier gas in air. A number of important observations were made. Plasma discharges in air in the absence of external opposing forces (i.e. forces which disturbed the flow) followed a straight trajectory with the axial flow leading the propagation of the carrier gas in air. The adhesion between the carrier gas and the nozzle walls induced a retarding force on the carrier gas flow, so the axial flow speed increased to compensate for the loss in the flow rate. A CAP discharge onto a skin layer led to the largest accumulation of OH species at the central part of the exposed area. The size of the exposed area decreased with increasing nozzle-to-skin distance, while the distribution of OH species on the skin (i.e. the shape of the exposed area) was asymmetric. The dispersion of OH species over the skin layer was provided by contour plots. The developed computational model and the obtained results would be useful for future development of plasma medicine using CAPs.

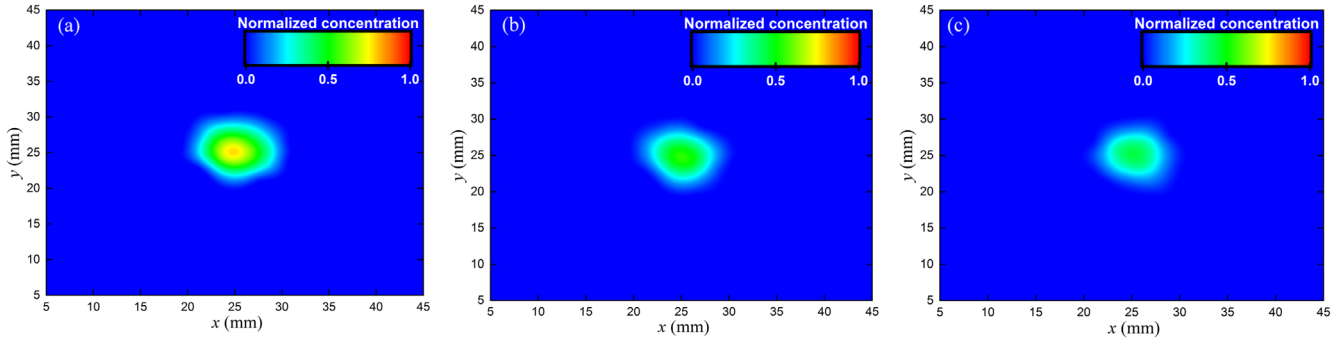


Figure 11. Spatial distributions of OH species over the skin layer for the flow rate of 1 L min^{-1} for nozzle-to-skin distances of (a) 3, (b) 4 and (c) 5 mm.

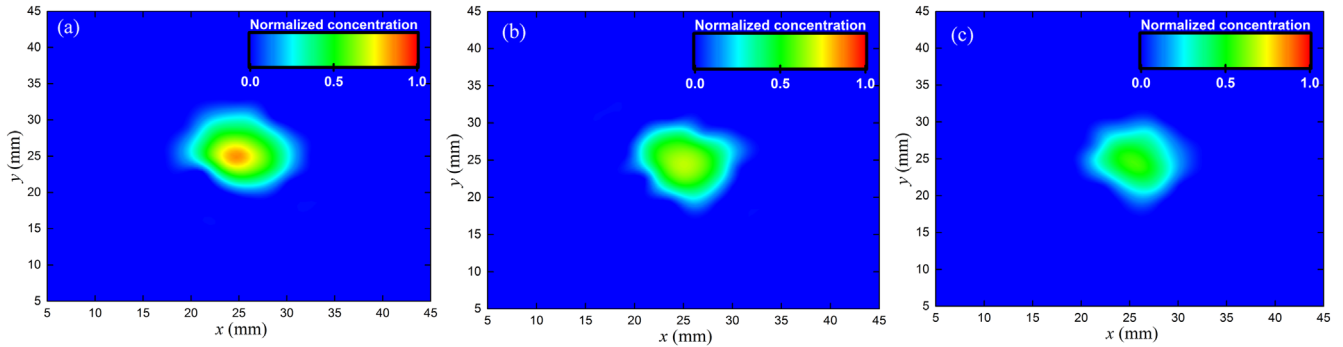


Figure 12. Spatial distributions of OH species over the skin layer for the flow rate of 2 L min^{-1} for nozzle-to-skin distances of (a) 3, (b) 4 and (c) 5 mm.

Acknowledgments

This work was funded by National Natural Science Foundation of China (Nos. U1632145, 81573093 and 81227902), a project funded by the Priority Academic Program Development of Jiangsu Higher Education Institutions (PAPD) and Jiangsu Provincial Key Laboratory of Radiation Medicine and Protection, China Postdoctoral Science Foundation (No. 2016M592584), and Strategic Research Grant 7004641 from City University of Hong Kong. We acknowledge the help from Dr Cheng Cheng and Ms. Jie Ma for taking photographs of plasma discharge, and the support of the Neutron computer cluster from the Department of Physics, City University of Hong Kong, for the computational work involved in this paper.

Appendix A

Here, we presented the generic analytical solution to the one-dimensional (1D) time-dependent diffusion equation and compared the results with our FEM model. For simplicity, we considered the diffusion of species along the x -axis in the Cartesian coordinate system. However, the present derivation could be further extended by the interested readers to a 3D coordinate system. The partial differential equation (PDE) that described the diffusion process (along the x -axis) was

$$\frac{\partial c}{\partial t} = D \frac{\partial^2 c}{\partial x^2} \quad (\text{A1})$$

where c was the concentration of the OH species that could be simply represented as $c(x, t)$ and D was the diffusion coefficient. The boundary conditions could be written as

$$c(x, 0) = C_0(x) \quad (\text{A2})$$

where $C_0(x)$ was the initial concentration of the OH species at t_0 , which was assumed to be valid over the modeled domain (i.e. along the x -axis). The two other boundary conditions were related to the modeled domain dimensions as shown in equations (A3) and (A4):

$$c(0, t) = c_L(t) \quad (\text{A3})$$

$$c(x_{\max}, t) = c_R(t). \quad (\text{A4})$$

The modeled geometry had a length from 0 to x_{\max} . For convenience, the modeled domain was assumed to start on the left (i.e. $x = 0$) while the maximum allowable length for OH species diffusion was at the other end of the modeled domain (i.e. $x = x_{\max}$). Here, c_L and c_R represented the concentration of OH species at the left and right ends of the modeled domain, respectively. Upon separation of the variables, we obtained

$$c(x, t) = X(x)\tau(t) \quad (\text{A5})$$

where $X(x)$ was only a function of x and $\tau(t)$ was only a function of time. Substituting equation (A5) into the right hand side (RHS) of equation (A1) would give

$$\frac{\partial c}{\partial t} = \frac{\partial [X(x)\tau(t)]}{\partial t} = X(x) \frac{\partial \tau(t)}{\partial t}. \quad (\text{A6})$$

Similarly, substituting equation (A5) into the left hand side

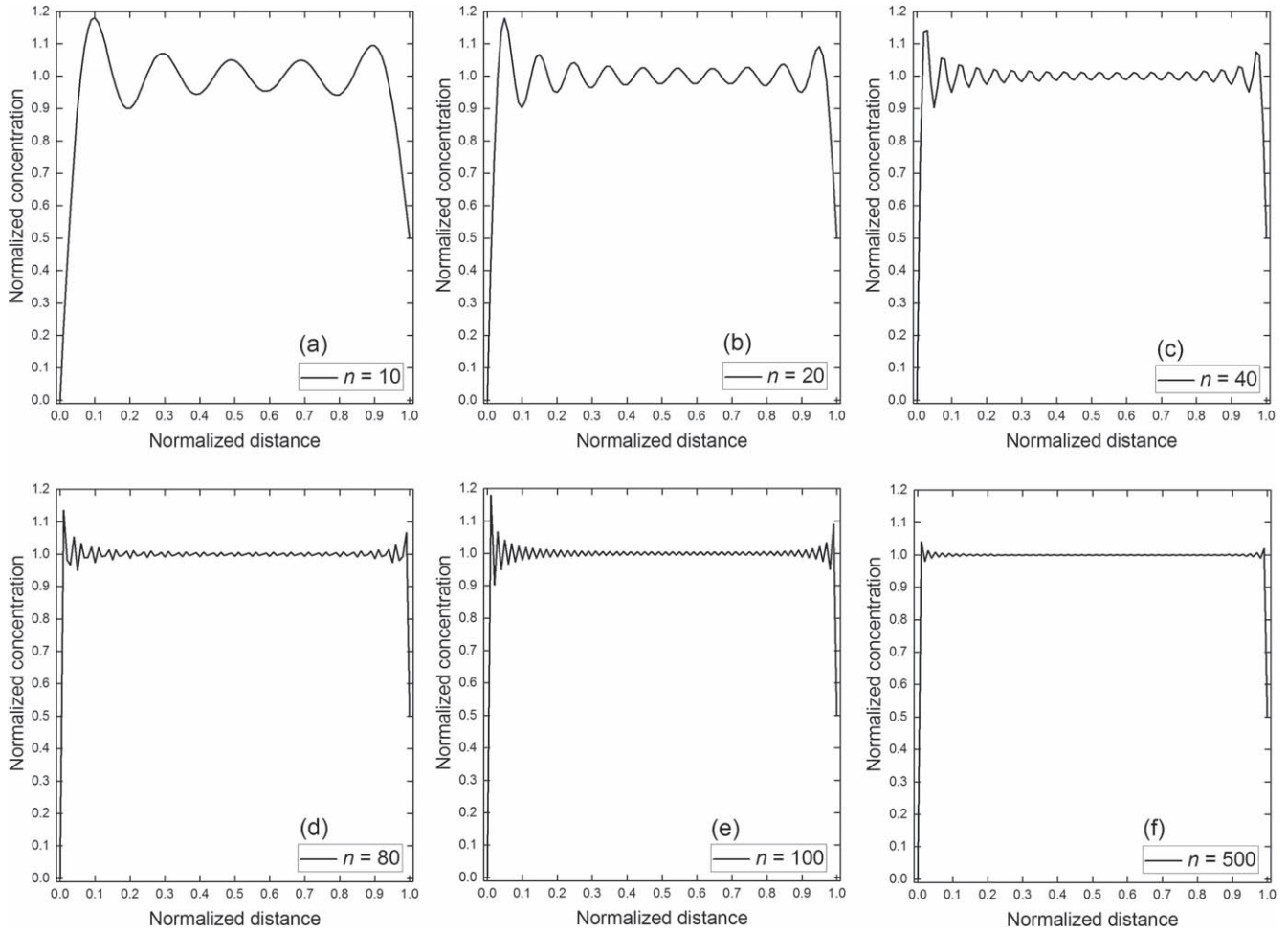


Figure A1. Variations in the convergence of the normalized concentrations at (a) $n = 10$, (b) $n = 20$, (c) $n = 40$, (d) $n = 80$, (e) $n = 100$ and (f) $n = 500$ at $t = 0$.

(LHS) of equation (A1) would give

$$D \frac{\partial^2 c}{\partial x^2} = \frac{D \partial^2 [X(x)\tau(t)]}{\partial x^2} = D\tau(t) \frac{\partial^2 X(x)}{\partial x^2}. \quad (A7)$$

The relation shown in equation (A1) would then lead to

$$X(x) \frac{\partial \tau(t)}{\partial t} = D\tau(t) \frac{\partial^2 X(x)}{\partial x^2}. \quad (A8)$$

Since $X(x)$ was only a function of distance and $\tau(t)$ was only a function of time, these variables could be separated as

$$\frac{1}{D\tau(t)} \frac{\partial \tau(t)}{\partial t} = \frac{1}{X(x)} \frac{\partial^2 X(x)}{\partial x^2}. \quad (A9)$$

The LHS and RHS of the equation shown in equation (A9) were functions of time and distance, respectively, which could thus be equated to a constant, denoted here as $-\alpha^2$:

$$\frac{1}{D\tau(t)} \frac{d\tau(t)}{dt} = -\alpha^2 \quad (A10)$$

$$\frac{1}{X(x)} \frac{d^2 X(x)}{dx^2} = -\alpha^2. \quad (A11)$$

The general solutions to equations (A10) and (A11) were

$$\tau(t) = Ae^{-\alpha^2 Dt} \quad (A12)$$

$$X(x) = [B \sin(\alpha x) + C \cos(\alpha x)]. \quad (A13)$$

The general solution to equation (A11) could be found using an auxiliary function. The obtained root would be imaginary. Using the general solution, $c(x, t)$ could be represented via substituting equations (A12) and (A13) as

$$c(x, t) = \tau(t)X(x) = Ae^{-\alpha^2 Dt} [B \sin(\alpha x) + C \cos(\alpha x)]. \quad (A14)$$

Equation (A14) could be further presented with constants C_1 and C_2 as

$$c(x, t) = e^{-\alpha^2 Dt} [C_1 \sin(\alpha x) + C_2 \cos(\alpha x)] \quad (A15)$$

assuming $c(0, t) = 0$, $C_2 = 0$. Similarly, when $c(x_{\max}, t) = 0$ was assumed,

$$c(x, t) = \sum_{n=1}^{\infty} B_n e^{-\alpha^2 Dt} \sin(\alpha_n x) \quad (A16)$$

where $\alpha_n = n\pi/x_{\max}$. $c(x, t)$ was further rewritten as

$$c(x, t) = v(x, t) + w(x). \quad (A17)$$

Since $v(0, t) = 0$ and $v(x_{\max}, t) = 0$, $w(0) = c(0, t) - v(0, t) = c_L - 0 = c_L$; and for x_{\max} , $w(x_{\max}) = c(x_{\max}, t) - v(x_{\max}, t) = c_R - 0 = c_R$. Hence, $w(0) = c_L$ and $w(x_{\max}) = c_R$. It was noted that w was only a function of x , so

$\partial w / \partial t = 0$, and thus

$$D \frac{\partial^2 w}{\partial x^2} = 0. \quad (\text{A18})$$

By integrating equation (A17) twice and applying the boundary conditions as $w(0) = c_L$ and $w(x_{\max}) = c_R$, the solution to $w(x)$ was found as

$$w(x) = \left(\frac{c_R - c_L}{x_{\max}} \right) x + c_L. \quad (\text{A19})$$

Using the relation proposed in equation (A17),

$$c(x, t) = v(x, t) + w(x) = \sum_{n=1}^{\infty} B_n e^{-\left(\frac{n\pi}{x_{\max}}\right)^2 Dt} \sin\left(\frac{n\pi x}{x_{\max}}\right) + \left(\frac{c_R - c_L}{x_{\max}} \right) x + c_L. \quad (\text{A20})$$

The expression for $v(x, t)$ represented the transient (i.e. time-dependent) term, whereas the expression for $w(x)$ represented the steady-state part of equation (A20). Assuming that $c(x, 0) = C_0$, where C_0 was a constant, the terms B_n could be presented as

$$B_n = \frac{2}{x_{\max}} \int_0^{x_{\max}} (f(x) - w(x)) \sin\left(\frac{n\pi x}{x_{\max}}\right) dx$$

$$n = 1, 2, 3, \dots \quad (\text{A21})$$

In equation (A20), the summation term went to infinity, which was in fact not feasible. Based on our analysis for $t = 0$, $c_L = 0$ and $c_R = 0.5$, we presented the results for different n values. At $t = 0$, the normalized concentration should be unity. The results shown in figure A1 showed that a good and reliable convergence could be achieved for $n = 500$.

References

- [1] Fridman G et al 2008 *Plasma Process. Polym.* **5** 503
- [2] Park G Y et al 2012 *Plasma Sources Sci. Technol.* **21** 043001
- [3] Laroussi M 2015 *IEEE Trans. Plasma Sci.* **43** 703
- [4] Lu X et al 2016 *Phys. Rep.* **630** 1
- [5] Lu X et al 2014 *Phys. Rep.* **540** 123
- [6] Graves D B 2014 *Phys. Plasmas* **21** 080901
- [7] Murakami T et al 2013 *Plasma Sources Sci. Technol.* **22** 015003
- [8] Ji L F et al 2013 *Appl. Phys. Lett.* **102** 184105
- [9] Nam S H et al 2013 *J. Appl. Oral Sci.* **21** 265
- [10] Foest R et al 2007 *Contrib. Plasma Phys.* **47** 119
- [11] Reuter R et al 2012 *Plasma Process. Polym.* **9** 1116
- [12] Murakami T et al 2014 *Plasma Sources Sci. Technol.* **23** 025005
- [13] Naidis G V 2014 *Plasma Sources Sci. Technol.* **23** 065014
- [14] Winter J, Brandenburg R and Weltmann K D 2015 *Plasma Sources Sci. Technol.* **24** 064001
- [15] Flynn P B et al 2016 *Sci. Rep.* **6** 26320
- [16] Naidis G V 2013 *Plasma Sources Sci. Technol.* **22** 035015
- [17] Ikawa S, Kitano K and Hamaguchi S 2010 *Plasma Process. Polym.* **7** 33
- [18] Laroussi M 2005 *Plasma Process. Polym.* **2** 391
- [19] Lee H W et al 2009 *J. Endod.* **35** 587
- [20] Laroussi M 2014 *Plasma Process. Polym.* **11** 1138
- [21] Kaushik N K et al 2013 *Curr. Appl. Phys.* **13** 176
- [22] Lu X, Laroussi M and Puech V 2012 *Plasma Sources Sci. Technol.* **21** 034005
- [23] Yue Y F, Pei X K and Lu X P 2017 *IEEE Trans. Radiat. Plasma Med. Sci.* **1** 541
- [24] Keidar M et al 2013 *Phys. Plasmas* **20** 057101
- [25] Kim G J et al 2010 *Appl. Phys. Lett.* **96** 021502
- [26] Ishaq M, Evans M D M and Ostrikov K 2014 *Biochim. Biophys. Acta Mol. Cell Res.* **1843** 2827
- [27] Kaushik N K, Uhm H and Choi E H 2012 *Appl. Phys. Lett.* **100** 084102
- [28] Ostrikov K, Neyts E C and Meyyappan M 2013 *Adv. Phys.* **62** 113
- [29] Keidar M and Beilis I I 2009 *J. Appl. Phys.* **106** 103304
- [30] Lu Q Q et al 2014 *Plasma Process. Polym.* **11** 1028
- [31] Xu D H et al 2015 *PLoS One* **10** e0128205
- [32] Cheng X Q et al 2014 *J. Phys. D Appl. Phys.* **47** 335402
- [33] Cheng X Q et al 2014 *PLoS One* **9** e98652
- [34] Yan D Y et al 2015 *Sci. Rep.* **5** 18339
- [35] Isbary G et al 2010 *Br. J. Dermatol.* **163** 78
- [36] Arndt S et al 2013 *PLoS One* **8** e79325
- [37] Noriega E et al 2011 *Food Microbiol.* **28** 1293
- [38] Perni S, Kong M G and Prokopovich P 2012 *Acta Biomater.* **8** 1357
- [39] Preedy E C et al 2014 *Colloids Surf. A Physicochem. Eng. Aspects* **460** 83
- [40] Li Y et al 2017 *Sci. Rep.* **7** 45781
- [41] Ishaq M, Evans M and Ostrikov K 2014 *Int. J. Cancer* **134** 1517
- [42] Lu X P and Ostrikov K 2018 *Appl. Phys. Rev.* **5** 031102
- [43] Schröder M, Ochoa A and Breitkopf C 2015 *Biointerphases* **10** 029508
- [44] Pei X K et al 2014 *IEEE Trans. Plasma Sci.* **42** 1206
- [45] Shahmohammadi Beni M and Yu K N 2017 *Math. Comput. Appl.* **22** 24
- [46] Shahmohammadi Beni M and Yu K N 2015 *Biointerphases* **10** 041003
- [47] Shahmohammadi Beni M and Yu K N 2017 *Appl. Sci.* **7** 578
- [48] Olsson E and Kreiss G 2005 *J. Comput. Phys.* **210** 225
- [49] Olsson E, Kreiss G and Zahedi S 2007 *J. Comput. Phys.* **225** 785
- [50] Shahmohammadi Beni M, Zhao J Y and Yu K N 2018 *Ann. Nucl. Energy* **113** 162
- [51] Liu D X et al 2010 *Plasma Sources Sci. Technol.* **19** 025018
- [52] Liu Y, Ivanov A V and Molina M J 2009 *Geophys. Res. Lett.* **36** L03816
- [53] Thoroddsen S T, Etoh T G and Takehara K 2007 *Phys. Fluids* **19** 042101
- [54] Yonemori S and Ono R 2014 *J. Phys. D Appl. Phys.* **47** 125401
- [55] Luan P S et al 2017 *J. Vac. Sci. Technol. A* **35** 05C315